Applied Optics, 2012, Volume 51, Issue 16, Pages 3478-3490

Objective speckle velocimetry for autonomous vehicle odometry

D. Francis,[1] T. O. H. Charrett,[1] L. Waugh,[2] and R. P. Tatam[1,*]

[1]Department of Engineering Photonics, School of Engineering, Cranfield University, Cranfield, Bedford MK43 0AL, UK

[2]EADS Astrium, Gunnels Wood Road, Stevenage, Hertfordshire SG1 2AS, UK

*Corresponding author: r.p.tatam@cranfield.ac.uk

Received 30 January 2012; revised 7 March 2012; accepted 7 March 2012; posted 8 March 2012 (Doc. ID 162299); published 31 May 2012

Speckle velocimetry is investigated as a means of determining odometry data with potential for application on autonomous robotic vehicles. The technique described here relies on the integration of translation measurements made by normalized cross-correlation of speckle patterns to determine the change in position over time. The use of objective (non-imaged) speckle offers a number of advantages over subjective (imaged) speckle, such as a reduction in the number of optical components, reduced modulation of speckles at the edges of the image, and improved light efficiency. The influence of the source/detector configuration on the speckle translation to vehicle translation scaling factor for objective speckle is investigated using a computer model and verified experimentally. Experimental measurements are presented at velocities up to 80 mm s^{-1} which show accuracy better than 0.4%. © 2012 Optical Society of America

OCIS codes: 100.2000, 120.6150, 120.7250.

1. Introduction

One of the key challenges in the development of the navigational capabilities of autonomous robotic vehicles is the accurate and reliable measurement of the position and velocity of the vehicle. The measurement of a vehicle's location is known as odometry (literally 'measurement of travel') and is conventionally achieved using rotary encoders in the wheels of the vehicle [1]. A rotary encoder consists of an LED (light emitting diode) and a detector within the wheel. Light from the LED is reflected from a pattern imprinted on the wheel consisting of alternating dark and light regions. The rotation of the wheel can be determined from the fluctuation in intensity observed by the detector and the change in position calculated from the wheel circumference. The current position of the vehicle is determined through integration of position measurements made by the encoders from a particular starting position in a process referred to as dead reckoning. Although wheel based odometry is simple and inexpensive it does suffer from a number of limitations, for example due to wheel slippages, unequal wheel diameters, misalignment of wheels, surface roughness, and rounding errors due to the discrete sampling of wheel increments [1]. This can lead to the accumulation of errors and large uncertainties in position, for instance, on the Mars exploration rover (MER) Spirit, an error of 3% from wheel encoders combined with a fibre-optic gyroscope based inertial measurement unit (IMU) was reported when travelling over 3 km of flat ground, but errors up to 125% were reported when travelling over uneven ground [2]. For walking vehicles the errors associated with optical encoders are even worse, typically achieving position errors of 5% to 25% [3]. Hence, there is considerable interest in the development of alternative odometry methods.

Besides interplanetary rovers, other applications of autonomous vehicles that require improved odometry include landmine detection robots [4,5],

1559-128X/12/163478-13$15.00/0

pipeline inspection robots [6], and robots involved in inspection, repair and decommissioning of nuclear facilities [7]. Detection and deactivation of in-ground landmines is an important but dangerous task, therefore autonomous robots are being developed to perform the task. Accurate odometry is important here to be sure that a region has been completely covered before it can be designated safe. A number of robots developed for landmine detection purposes are walking robots to help overcome difficult terrain and hence wheel odometry cannot be relied upon. One system has reported a solution using a ground facing camera which detects landmarks and tracks the shift in the features as the robot moves [4].

To overcome the limitations of reliance on wheel odometry alone, many robotic applications utilize visual odometry [8]. This technique involves recording images of the scene through which the vehicle is traversing. The images are pre-processed to remove lens distortion and then significant features within the image are selected and tracked from one image to the next to build an optical flow field [9]. The motion of the camera is then determined from the optical flow field after it has been checked for errors. Visual odometry has been successfully demonstrated on the MER platforms [10] using a stereoscopic pair of cameras. Use of stereo cameras also provides depth information and on the Mars rover is also used for route planning. Due to the computational complexity of the image processing algorithms involved, the visual odometry capability was only activated during times when the wheel encoder/IMU combination struggled, such as when climbing steep slopes. Position errors of 1.5% to 2.5% were obtained using visual odometry even in the presence of the large slips that caused the large uncertainties in the encoder/IMU measurements quoted previously. A recent publication [6] investigated two algorithms for monocular visual odometry for pipeline inspection robots and achieved an accuracy of better than 1%.

Global positioning systems (GPS) are often used to provide an alternative means of determining a vehicles locality [11]. However, in many application areas this is not available or practical, for example interplanetary rovers or vehicles operating underground or indoors such as pipeline inspection vehicles or nuclear decommissioning robots.

The inclusion of speckle velocimetry into the family of odometry techniques is a relatively new one. The technique measures a vehicles motion from the translation of laser speckle patterns. It has been used previously on an Antarctic rover [12]. The advantage of speckle velocimetry is that it can be used successfully even when there are no features, a situation which would limit related techniques such as visual odometry or digital image correlation. Other advantages of speckle velocimetry include the ability to make accurate measurements in the presence of slippages and skids as well as when the vehicle is stationary and has simpler image processing requirements than currently used in visual odometry. Previously, we assessed speckle velocimetry as a suitable approach to odometry with particular application for planetary exploration rovers [13]. The technique used subjective (imaged) speckle patterns and proved to be successful at velocities below 1 mm s^{-1} with errors of around 0.2% demonstrated. In this publication we describe the development of a speckle velocimetry based odometry system that uses objective (non-imaged) speckle patterns, and present results made at a maximum velocity of 80 mm s^{-1}, which is typical of a number of autonomous robotic vehicles. For instance the MER rovers have a maximum velocity of 50 mm s^{-1}, the European Space Agency's ExoMars rover is expected to have a maximium velocity of 85 mm s^{-1}, and the walking demining robot constructed in the DYLEMA project has a body speed of 50 mm s^{-1} [5]. The two different speckle types are discussed further in Subsection 2.A.

2. Speckle Velocimetry

The principle of speckle velocimetry is illustrated in Fig. 1. A laser mounted on the vehicle illuminates a region of the ground over which the vehicle is travelling and forms a laser speckle pattern (see Subsection 2.A). The speckle pattern is viewed by a camera which is also mounted on the vehicle. Provided the movement of the vehicle between frames is small, the speckle pattern translates rigidly. The translation of the speckle pattern in the image plane between consecutive images is calculated and then scaled to determine the translation of the vehicle. The change in position of the vehicle from a particular starting point is found through integration of translation measurements. There are a number of techniques that can be used for computing speckle translation, such as the optical flow algorithms [9]

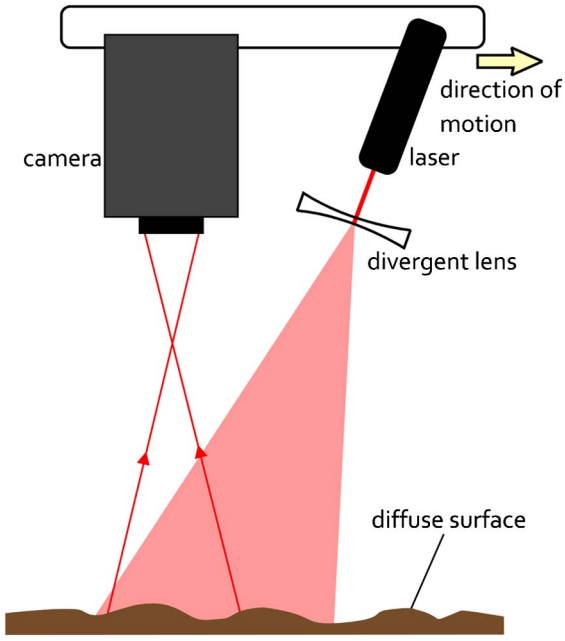

Fig. 1. (Color online) The principle of speckle velocimetry.

or Radon transformations [12]. Our previous study [13] concluded that the normalized cross-correlation was the most suitable for this application. The normalized cross-correlation is described in Subsection 2.B.

The development of an odometry system based on speckle velocimetry presents a number of challenges. In particular, to operate successfully at the speeds typical of autonomous vehicles a high camera frame rate is required to ensure that the speckle pattern translation is nominally rigid between images and that most of the features remain within the image between frames. A high frame rate requires a short exposure time and a short exposure time is also necessary to limit blurring of the speckle pattern. The need for a short exposure time puts constraints on the amount of light required to provide adequate signal at the detector. The signal level is dependent on the power of the laser, the area of illumination, the reflectivity of the surface, the distance between the detector, and the surface and the sensitivity of the detector. The average speckle size within the pattern is also a consideration and control of the speckle size is required since in order to properly sample the pattern there should be at least two pixels per speckle [14]. This refers to the size in both x and y directions so 2×2 pixels^2 is required. The formation of speckle and the resulting speckle size is discussed further in Subsection 2.A.

A. Laser Speckle

Laser speckle is formed by the interference of scattered light reflected from (or transmitted through) a surface whose topographical features are greater than the optical wavelength. The contrast of the speckle pattern is dependent on the coherence of the light used. Speckle patterns that are produced using polarized light with high temporal and spatial coherence, such as laser light, from a relatively large illuminated area are said to be *fully developed* or 'normal' speckle patterns and share the same statistical properties [15]. A laser speckle pattern exists in the space surrounding the illuminated area. The speckle pattern observed on a screen, which could be photographic film or an electronic detector for instance, intercepting scattered light at some distance from the illuminated region, is known as an objective speckle pattern. The formation of an objective speckle pattern is shown in Fig. 2(a). The average speckle size in an objective speckle pattern is given by [16]

$$\langle \sigma_O \rangle = \frac{\lambda L}{A}, \tag{1}$$

provided the ratio of the observation distance L to the diameter of the illuminated area A is large enough that the small angle approximation can be applied. If a lens is used to image the speckle pattern onto the detector, a subjective speckle pattern is formed, as shown in Fig. 2(b). This pattern is termed subjective because the pattern that is produced is dependent on the parameters of the imaging optics used. The average speckle size in a subjective speckle pattern is given by [16]

$$\langle \sigma_S \rangle = \lambda \frac{F(1+M)}{a}, \tag{2}$$

provided the lens is diffraction limited. Here F/a is the F-number of the lens (focal length over aperture) and M is the magnification.

There are a number of factors to consider when choosing which speckle type (objective or subjective) to use for speckle velocimetry. Since an average speckle size greater than twice the pixel size is required to adequately sample the speckle pattern [14] an imaging system with quite a high F-number is often required for subjective speckle. This small aperture cuts out a lot of the available light resulting in a reduced signal level at the detector. In contrast, the signal level and average speckle size for objective speckle are dependent on the configuration used and this can be adjusted to achieve a good balance between signal and speckle size. The speckle translation to vehicle translation scaling factor can be determined simply by measurement of the field of view in the case of subjective speckle, but in the case of objective speckle it is more complicated and dependent on the configuration. This issue will be discussed in Subsection 2.C and Section 3. Another difference is that the illumination area is usually somewhat smaller in the case of objective speckle than for subjective, typically a few millimeters compared to tens of millimeters. This is because the average speckle size is controlled by the illuminated area in the objective

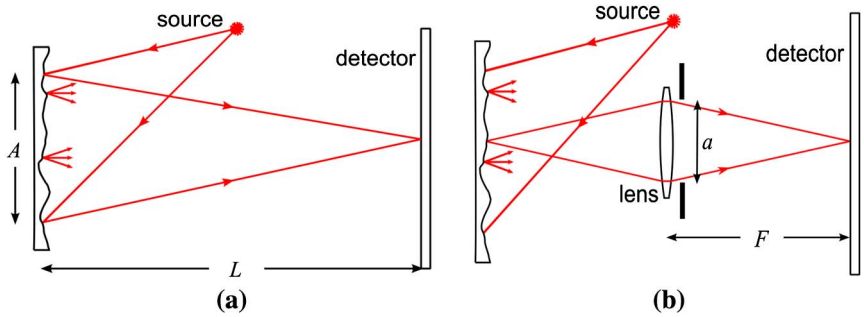

Fig. 2. (Color online) Formation of objective speckle (a) and subjective speckle (b).

case and in the subjective case the illuminated area should overfill the field of view to minimize background intensity variations arising due to the Gaussian profile of the laser beam. These considerations are summarized in Table 1.

Other advantages of objective speckle include a reduction in the number of components required, resulting in a simpler instrument. Also, since a smaller proportion of the speckle pattern is acquired, translation of the camera and source results in less change in the part of the pattern observed by the camera, so a greater translation between frames can be tolerated.

B. Normalized Cross-Correlation

Cross-correlation is a convolution based operation that can be used to provide a measure of the similarity of two distinct functions. In contrast, the correlation of a function with itself is known as auto-correlation. Cross-correlation is used in image processing for applications such as feature detection, matching and calculation of the translation of features from one image to the next. The discrete 2-D cross-correlation can be expressed as [17]

$$\gamma(u,v) = \sum_{x,y} f(x,y)t(x-u,y-v), \tag{3}$$

where f is the image and t is the template that is being searched for at each coordinate location (u,v) and is the same size or smaller than f. It can be solved using a fast Fourier transform algorithm by

$$\gamma(u,v) = F^{-1}\{F(f)F^{*}(t)\}, \tag{4}$$

where F denotes the Fourier transform operation and the $*$ represents the complex conjugate. However, this result is a simplification and in circumstances where there is variation in the intensity of the images feature matching may fail. The problem can be addressed by using the normalized cross-correlation, which can be expressed as [17]

$$\gamma(u,v) = \frac{\sum_{x,y}[f(x,y)-\overline{f}_{u,v}][t(x-u,y-v)-\overline{t}]}{\left\{\sum_{x,y}[f(x,y)-\overline{f}_{u,v}]^2\sum_{x,y}[t(x-u,y-v)-\overline{t}]^2\right\}^{0.5}}. \tag{5}$$

Figure 3 illustrates the process of normalized cross-correlation on a pair of computer generated speckle patterns. The features in the template t are shifted by 20 pixels to the right relative to those in the image f. The result of the normalized cross-correlation (NXC) is a third image with a peak located at the point where the features are most closely matched. Due to the discretisation into pixels of the optical signal in digital imaging, the result of the cross-correlation will be biased towards integer pixel shifts resulting in an error source known as peak locking. A simple method of achieving sub-pixel accuracy is to apply Gaussian interpolation to the correlation peak using [18]

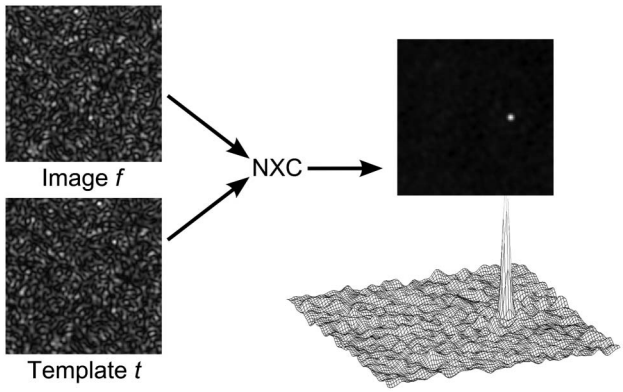

Fig. 3. Principle of normalized cross-correlation (NXC). The peak in the resulting image corresponds to the point where the features of the template, t most closely match those of the image, f.

$$p_x = x + \frac{\ln[\gamma(x-1,y)]-\ln[\gamma(x+1,y)]}{2\ln[\gamma(x-1,y)]-4\ln[\gamma(x,y)]+2\ln[\gamma(x+1,y)]},$$
$$p_y = y + \frac{\ln[\gamma(x,y-1)]-\ln[\gamma(x,y+1)]}{2\ln[\gamma(x,y-1)]-4\ln[\gamma(x,y)]+2\ln[\gamma(x,y+1)]}, \tag{6}$$

where $\gamma(x,y)$ is the peak value of the normalized cross-correlation distribution calculated using Eq. (5).

C. Correlation of Speckle Patterns for In-Plane Displacement Measurement

The use of interferometric laser speckle for high sensitivity micro-scale measurement of surface displacement and strain is well established [19]. These techniques require that the displacement is not to the extent that the speckles in one image are no longer spatially matched with the speckles in the previous image. If this is the case, the speckle pattern is said to become decorrelated and would no longer provide an accurate measurement. Digital speckle photography (DSP) [20] is a non-interferometric technique that utilizes the decorrelation of the speckle pattern to measure displacement. As such, it is complementary to speckle interferometry as it is suitable for measurements of larger displacements (from about 10 to 1000 μm). The principle of DSP involves recording

Table 1. Summary of Parameters Pertinent to Choice of Speckle Type for Velocimetry Applications

Parameter	Objective Speckle	Subjective Speckle
Signal	Dependent on configuration.	Dependent on F-number of imaging lens.
Scaling factor	Dependent on configuration.	Can be determined from measurement of field of view.
Illumination beam divergence	Relatively small to control speckle size.	Relatively large to overfill field of view.

speckle patterns before and after the scattering object is displaced. Displacement measurements are made at different locations in the image by digital crosscorrelation of image subsets to create a displacement vector map. The spatial resolution of the displacement map is inversely proportional to the size of the image subsets. Using a single imaging sensor, DSP can be used to determine the two in-plane components of displacement. By using two cameras to create a stereoscopic system, the out-of-plane displacement component can also be determined [21].

The study of displacement and decorrelation of speckle fields due to object surface translation has long been of interest to researchers. In 1981, Yamaguchi [22] derived equations that relate the speckle translation coefficient, which can be calculated using cross-correlation, to the translation, rotation, and strain of the surface, for both objective and subjective speckle. Later, Horváth *et al.* used a different approach to determine these relationships for objective [23] and subjective [24] speckle and applied them to in-plane and out-of-plane translation measurements [25]. Measurement of object translation using speckle correlation has been extended to measure in-plane velocities [26]; however, the velocity range that was measured (10–150 μm s^{-1}) is much lower than that typical of autonomous vehicles.

In the case of objective speckle, the pattern translation A_x and A_y is related to the object translation (a_x, a_y, a_z), the object rotation $(\Omega_x, \Omega_y, \Omega_z)$ and the strain tensor $(\varepsilon_{xx}, \varepsilon_{yy}, \varepsilon_{zz})$ by [22,23]

$$\begin{aligned} A_x = &-a_x\left[\frac{L_D}{L_S}(l_{Sx}^2 - 1) + l_x^2 - 1\right] - a_y\left[\frac{L_D}{L_S}l_{Sx}l_{Sy} + l_x l_y\right] \\ &- a_z\left[\frac{L_D}{L_S}l_{Sx}l_{Sz} + l_x l_z\right] - L_D[\varepsilon_{xx}(l_{Sx} + l_x) \\ &+ \varepsilon_{xy}(l_{Sy} + l_y) + \Omega_z(l_{Sy} + l_y) + \Omega_y(l_{Sz} + l_z)], \\ A_y = &-a_x\left[\frac{L_D}{L_S}l_{Sx}l_{Sy} + l_x l_y\right] - a_y\left[\frac{L_D}{L_S}(l_{Sy}^2 - 1) + l_y^2 - 1\right] \\ &- a_z\left[\frac{L_D}{L_S}l_{Sy}l_{Sz} + l_y l_z\right] - L_D[\varepsilon_{yy}(l_{Sy} + l_y) \\ &+ \varepsilon_{xy}(l_{Sx} + l_x) + \Omega_z(l_{Sx} + l_x) + \Omega_x(l_{Sz} + l_z)], \end{aligned} \tag{7}$$

where L_S and L_D are the source-object and object-to-detector distances, respectively, and (l_{Sx}, l_{Sy}, l_{Sz}) and (l_x, l_y, l_z) are unit vectors in the source-object and object-detector directions, respectively. It is therefore apparent that for a purely in-plane displacement, the magnitude of the speckle displacement is dependent not only on the object displacement, but the illumination and observation configuration of the measurement system. This relationship is investigated further in Section 3.

3. Computational Investigation of Speckle Translation

In speckle velocimetry, the scattering surface is stationary and it is the camera and source that are displaced. This case is mathematically equivalent to the case described in Eq. (7) with the strain tensor equalling zero. In order to calculate the change in position of the camera sensor, and hence the vehicle it is fixed to, the relationship between the measured speckle displacement and the translation of the camera needs to be determined. The scaling factor is the ratio of the speckle translation to vehicle translation and is dependent on the illumination and observation configuration as discussed in Subsection 2.C.

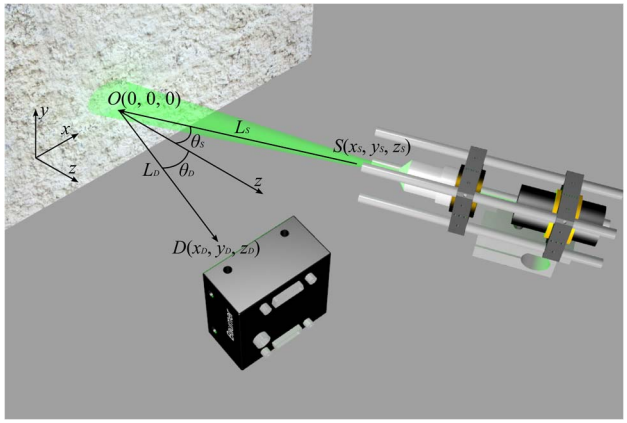

Fig. 4. (Color online) Coordinate system used for the speckle model, showing the location of the laser point source S, the origin at the centre of the illuminated region on the object O, and the centre of the detector array D.

A. Modeling of Laser Speckle

To investigate how the configuration affects the scaling factor a computational model was developed using Matlab. Laser light was considered to diverge from a point source located at $S(x_S, y_S, z_S)$, as shown in Fig. 4. The path lengths from S to a circular illuminated area on the scattering surface centerd at the origin of the coordinate system $O(0, 0, 0)$ were calculated. The number of illuminated points was selected ($\sim$10,000) to give good computational efficiency while having sufficient points to produce a fully-developed speckle pattern. The path lengths from each point in the illuminated region to each pixel in the detector array centerd at $D(x_D, y_D, z_D)$ were computed. The complex amplitude incident on the sensor array was calculated from these path lengths using [15]

$$E(x, y) = \sum^{N} a_j \exp(i\phi_j) \exp\left(\frac{i2\pi}{\lambda} \cdot \mathrm{PL}\right), \tag{8}$$

where N is the number of scattering points on the object's surface, a_j are random variables representing the amplitude scattered from the rough surface and ϕ_j are random variables independent of a_j representing the phase of light scattered from the rough surface and are uniformly distributed in the range $-\pi$ to $+\pi$. PL is the path lengths calculated previously. The intensity of the speckle pattern is obtained through

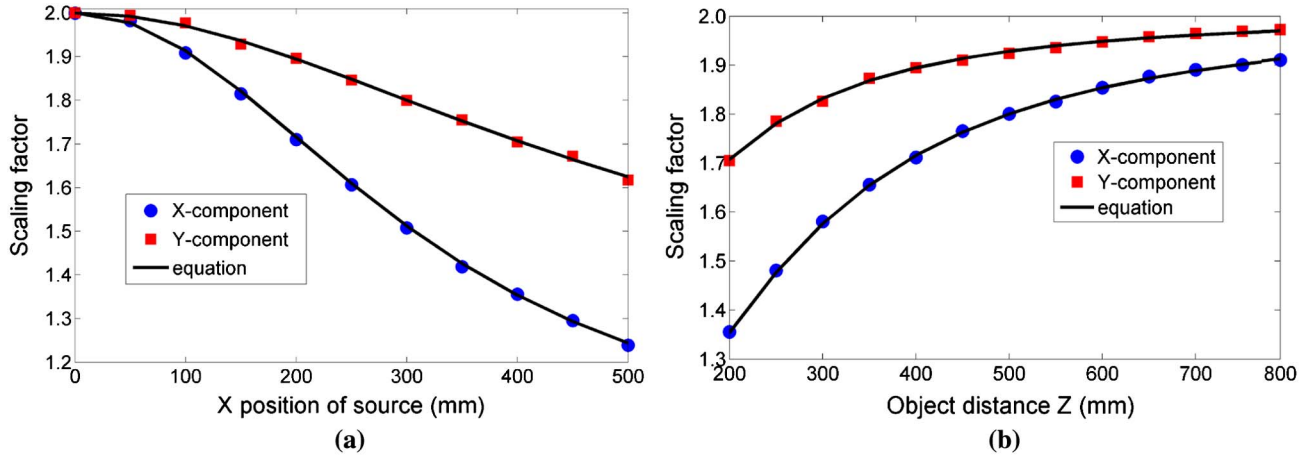

Fig. 5. (Color online) Plots showing the variation in scaling factor with increasing detector-source separation (a) and increasing object distance (b). The square (red) and circle (blue) points were calculated using the speckle model and normalized cross-correlation and the solid lines by Eq. (10).

$$I(x,y) = E(x,y) \cdot E^*(x,y). \tag{9}$$

The speckle patterns shown in Fig. 3 were produced using this model. The square root of the intensity is shown to improve the dynamic range for display purposes. The model takes roughly 60 seconds to generate a single 150×150 speckle pattern using a 2.93 GHz dual-core PC with 4 GB RAM.

B. Investigation of Speckle Translation with Model

In the investigations described here, the rotation and out-of-plane motion are not considered and there is assumed to be no surface strain to consider, therefore Eq. (7) can be significantly simplified. Assuming the source and detector lie in the x-z plane ($y_S = 0$ and $y_D = 0$ in Fig. 4), the relationship between the speckle translation and the object translation is given by [25]

$$A_x = a_x\left(\frac{L_D \cos^2\theta_S}{L_S \cos\theta_D} + \cos\theta_D\right), \; A_y = a_y\left(\frac{L_D}{L_S} + 1\right), \tag{10}$$

where θ_S and θ_D are the illumination and observation angles, respectively.

The influence of the angular position of the source was investigated using the speckle model described in Subsection 3.A and compared with Eq. (10). The detector, D was located on the z axis 400 mm away from O and oriented at normal incidence ($\theta_D = 0$). The detector consists of an array of 150×150 pixels each 10 μm square. The source, S is initially located at the same position as the detector and as such the illumination and observation directions are collinear. Light from the source was considered to diverge to encompass a circular region with a radius 6 mm centred at O. The speckle pattern arising with the source and detector in these positions is calculated using the model. The positions of the source and detector are translated by 100 μm in the x-direction and another speckle pattern is produced. The normalized cross-correlation is calculated between the two modelled images and the translation is found. The process is then repeated with the translation in the y-direction. In this case, the speckle translation was found to be 20 pixels, which is twice the translation applied to the detector and source, in both the x and y directions and corresponds to a scaling factor of 2.0. This process was repeated with the point source positioned at different locations along the x-axis from 0 to 500 mm in steps of 50 mm. The scaling factor, and therefore the sensitivity to translation, is observed to decrease as the angular separation of the observation and illumination direction increases, as shown in Fig. 5(a). This effect is more pronounced when the shift is in the x-direction since D and S both lie in the xz plane.

Another investigation involved varying the position of the detector and source along the z-axis from 200 to 800 mm in steps of 50 mm. The point S was located 200 mm away from D along the x-axis at each point. The scaling factor was observed to increase with increasing object distance, as shown in Fig. 5(b). This is due to the angle between the observation and illumination directions decreasing as the source and detector move further from the object surface.

The scaling factor is also observed to be dependent on the z-axis separation of the source and detector. Figure 6 shows the variation in the scaling factor that occurs when the detector is kept fixed at 400 mm on the z-axis from O and the position of S on the z-axis is varied from 200 to 600 mm. The plot shows traces for two lateral positions of the source, at 50 mm on the x-axis [triangles (cyan) and diamonds (magenta)] and 200 mm on the x-axis [squares (red) and circles (blue)]. The scaling factor is greater for cases where the source is closer to the surface than the detector and increases when the angle between the illumination and observation directions is smaller.

The scaling factor, and hence the sensitivity to translation, can be used to influence the choice of configuration. For instance placing the source close to the surface with the camera further away and a

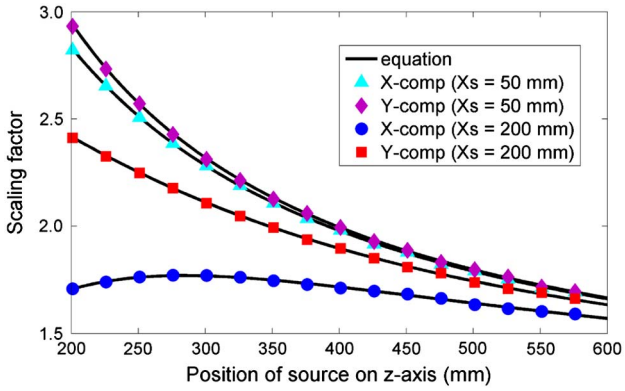

Fig. 6. (Color online) Plots showing the variation in scaling factor with the detector kept fixed at 400 mm and varying the vertical source position. The points were calculated using the speckle model and normalized cross-correlation and the black lines by Eq. (10).

relatively small angular separation would result in a system with high sensitivity. For example, with S at (50, 0, 200) and D at (0, 0, 400) a scaling factor approaching 3 is achieved, resulting in almost three times as much image plane shift as object plane shift. However, there are other considerations, for instance the configuration described above would be less light efficient than one where the detector is located closer to the surface.

4. Experimental Investigations

To investigate speckle velocimetry for the purpose of odometry, a test system was designed and constructed. It consisted of a frame which was used to support a pair of linear translation stages, as shown in Fig. 7. The red sand texture used in the figure was taken from [27]. The frame was built using Flexlink components and occupied about 1 m^3. The stages were a pair of Aerotech Pro115 linear translation stages arranged in an 'XY configuration'. The stages offer 400 mm travel and have a maximum velocity of 300 mm s^{-1} with a positioning accuracy of ± 12 μm. The stages were controlled using a pair of Ensemble™ MP drivers over an Ethernet network. A 'T' shaped aluminium plate was mounted onto the stage table of the lower 'X-axis' stage which was used to hold a sensor module consisting of a camera and laser. The camera was a Baumer HXC-13 CMOS camera, which offers excellent sensitivity and dynamic range (ISO2500, 90 dB) thanks to its large sensor. The sensor consists of 1024 × 1280 pixels each 14 μm^2 with data output in either 8- or 10 bit. The camera can provide a maximum frame rate of 500 FPS (frames-per-second) at full frame using a Full Camera Link® interface. The frame rate can be increased considerably by using a smaller region of interest. Data transfer was done using a National Instruments NI-PCI-1433 frame grabber card in a PC with an AMD Phenom II 6-core processor and 4 GB of RAM. The laser was a Photop DPGL-3020 DPSS module emitting 20 mW of radiation at 532 nm. The laser was mounted using Microbench™ and could rotate about two orthogonal axes to allow control over the illumination direction.

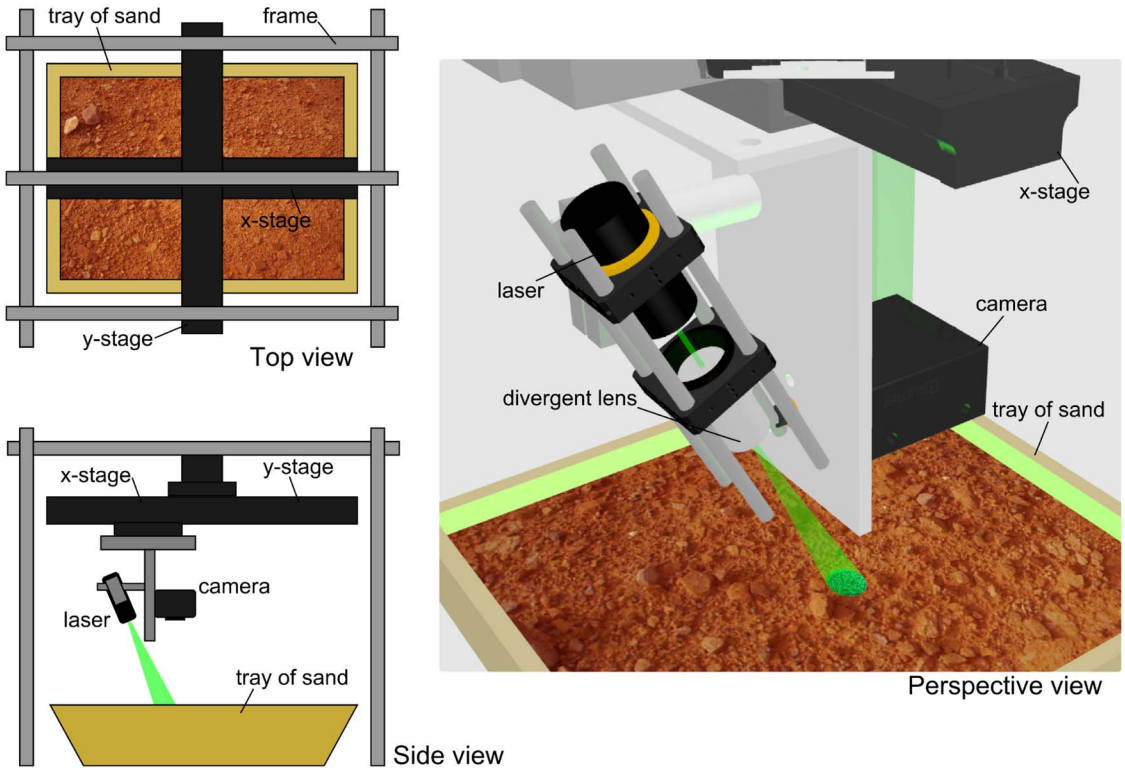

Fig. 7. (Color online) Schematic illustrating the design of the test system. The volume of the frame is approximately 1 m^3 and the distance between the camera/laser and the sand approximately 0.5 m [red sand texture from (27)].

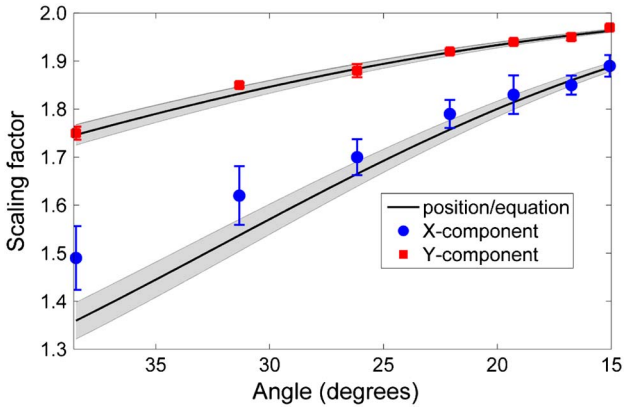

Fig. 8. (Color online) Variation in scaling factor against angular separation of the observation and illumination directions. The laser-camera separation was kept fixed at 140 mm and the angle altered by varying the height of the laser and camera. The points correspond to calibrations made with the test system and the continuous lines correspond to measurements of observation and illumination positions and are calculated using Eq. (10).

The control and processing software was developed using LabVIEW™. The program could be used to send commands to the stages over the Ethernet network. These could be either simple, single component commands or more complex pre-planned routes written in AeroBASIC™. Camera settings such as frame rate, exposure time, digital gain, and region of interest could also be adjusted in the software. The normalized cross-correlation was programmed in C++ using the FFTW [28] Fourier transform libraries, and was called from the main program using a DLL (dynamic link library).

A. Scaling Factor Investigations Using the Test System

The test system was used to verify the variation in scaling factor observed with the speckle model described in Subsection 3.A. The stages were used to translate the camera and laser at a speed of 1 mm s^{-1} for a distance of 10 mm. The total translation was determined by summing translation measurements made using normalized cross-correlation with Gaussian sub-pixel interpolation Eq. (6). A 128 × 128 region of interest was used and correlation of successive images was performed in real-time at a rate of approximately 35 correlations per second. This was repeated ten times each for translations in both the x and y directions and the average total translation was used to determine the scaling factor. This value was then compared with the scaling factor found from measurements of the observation and illumination positions and Eq. (10). The object distance z was varied by raising the tray of sand and the experiments were repeated. The lens-camera separation was kept fixed at 140 mm throughout, but the illumination direction was changed to ensure that the beam spot at the surface was positioned at the centre of the fieldof-view of the camera. This was verified by attaching an imaging lens to the camera before each test.

The variation in the scaling factor is shown in Fig. 8 plotted here against the decreasing angle between the observation and illumination directions. The circles and squares correspond to the scaling factor calculated from the translation measurements made with the test system for x and y translations, respectively. The error bars on the translation measurements were obtained from the standard deviation of the ten repetitions. The solid black lines correspond to the scaling factor calculated using Eq. (10) based on a lens-camera separation of 140 mm and the −40 mm negative lens to diverge the laser beam. The scaling factor variation shown here is different to the result of the model [Fig. 5(b)] due to it being plotted against angle here rather than object distance. This is because the angle varies non-linearly with increasing object distance. The shaded error bars on the equation curves were obtained assuming a ±5 mm accuracy on the position measurements. At shorter object distances there is a greater uncertainty in the scaling factor as can be seen from the difference between the two scaling factor measurements. This is highlighted by the large standard deviations apparent at shorter object distances, particularly for translation in the x-direction due to the camera and laser lying in the x-z plane. Indeed, the standard deviations at longer object distances for translations in the y direction are smaller than the point shown in the figure. The uncertainty in the scaling factor is also greater for a particular error in position measurement at shorter object distances. It is therefore apparent that to minimize the uncertainty in the scaling factor the angle between the observation and illumination direction should be minimized.

The measurements were repeated with the camera-to-laser separation reduced to 65 mm, which was the minimum that could be achieved using the 'T' bracket mount. The variation in scaling factor is shown in Fig. 9, plotted on the same scale as Fig. 8. The standard deviation of the translation measurements, shown in the error bars of the points, is now noticeably reduced for the x-component measurements, compared with Fig. 8 and is closer to the values for the

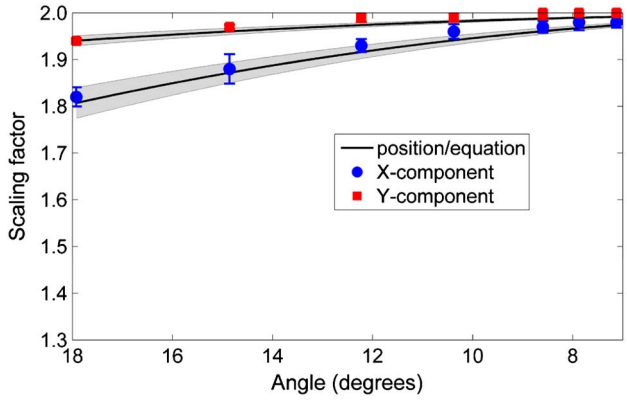

Fig. 9. (Color online) Variation in scaling factor against angular separation of the observation and illumination directions. The laser-camera separation was kept fixed at 65 mm and the angle altered by varying the height of the laser and camera.

y-component measurements at larger object distances, where the scaling factor approaches 2.0.

B. Odometry Trials Using the Test System

Odometry was performed using a pre-programmed path that followed an 'S' shape. Figure 10(a) shows the path calculated from data from the built-in encoders in the stage after traversing the 'S' at a maximum velocity of 3 mm s^{-1}. The start position is at (0,0) on the plot and the stages begin to move along the x-axis for 160 mm and then 100 mm along the y-axis (as indicated by the arrows), and then follow the rest of the path back to the starting point at (0,0), a total distance of 1.12 m. The variation in position and velocity over the duration of the traverse is shown in Figs. 10(b) and 10(c), respectively.

The experimental configuration was chosen based on the analysis described in Subsection 3.B. The angle between the observation and illumination directions was minimized by keeping the camera-laser separation fixed at 65 mm. This was the minimum separation that could be achieved using the T-shaped mounting bracket illustrated in Fig. 7. The distance between the surface and the laser and camera was set at approximately 210 mm. The angular separation between the observation and illumination directions could be reduced further by increasing this distance, but at the cost of decreased signal levels. The choice of 210 mm was made because it provided a good compromise between scaling factor stability and adequate received light levels.

Figure 11(a) shows a plot of the path determined by normalized cross-correlation of images acquired as the stages moved. Translation measurements obtained from successive images were integrated to produce the data for the plot. The quality of the correlation, termed the correlation Q-factor, was defined as the ratio of the highest value to the average value of the correlation image. If the value of the Q-factor was below a certain threshold, the translation measurement was rejected and the value of the previous translation measurement was used instead. A relatively strict threshold of 5 was chosen to ensure that no values from unsuccessful correlations were present in the final result. However, is should be noted that the data rate from speckle velocimetry is high, with the measurements per second potentially being as high as the camera frame rate, so discarding poor correlations is not a problem. At this velocity a relatively long exposure time (~4 ms) could be chosen in order to maximise the contrast of the speckle pattern since blurring of the speckle due to the motion was minimal. Therefore, the correlation Q-factor was generally quite high during motion (typically >20)

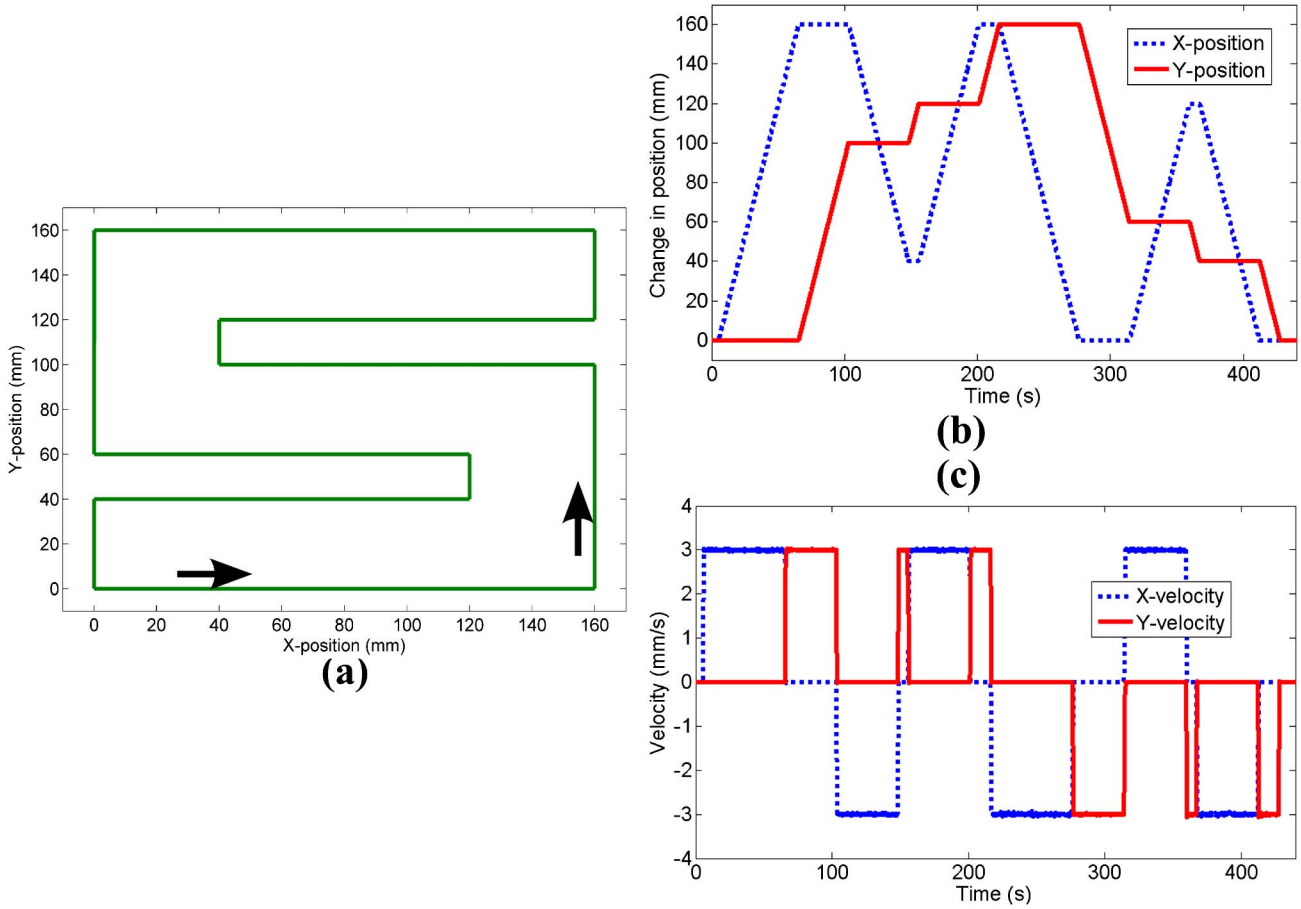

Fig. 10. (Color online) Path traversed by stages (travelling at 3 mm s^{-1}) calculated from the feedback from the stage encoders (arrows indicate direction of travel) (a). The change in position (b) and velocity (c) of the x-axis stage (dashed-blue) and y axis stage (continuous-red).

and only a few correlations fell below threshold. The noise present in the velocity measurements in Fig. 11(c) relative to those shown in Fig. 10(c) is due to the stepper motors in the stages regulating the velocity to keep the average velocity constant. It is observed in the cross-correlation measurements because they are of a higher temporal resolution than the feedback data from the stage encoders.

Measurements performed at 3 mm s^{-1} could be made in real-time by calculating the normalized cross-correlation between successively captured speckle patterns at a rate of approximately 35 correlations per second for 128 × 128 8 bit images. At higher stage velocities this rate is not sufficient and measurements can no longer be made in realtime. The limiting factor is the processing time for the cross-correlation operation. Instead, at higher velocities, speckle patterns were acquired at the camera frame rate and stored in a memory buffer for a preset duration that was known to exceed the duration of the traverse. After this period the buffered images were written to an .avi (audio/visual interleaved) movie file and the normalized cross-correlation between successive frames was performed as a post-process. This method has an advantage in that since the movie file is saved it can be processed in different ways later on. To run measurements for longer than the memory buffer allows, a cyclic buffer could be used, where after a certain number of frames have been acquired, older ones are overwritten. The cross-correlation operation would be required to run in parallel with image acquisition with the frequency of translation measurements being limited by the maximum correlation rate (35 per-second for this setup) and the velocity assumed to be constant between two correlations.

Figure 12(a) shows the path calculated from cross-correlation measurements when the stages are moving at a maximum velocity of 80 mm s^{-1}. The speckle patterns from a pair of successive frames in the movie file is shown in Fig. 12(b) and 12(c) and the normalized cross-correlation between them is shown in Fig. 12(d). The camera sensor was at a height of 200 mm above the surface of the sand and a –40 mm negative lens was used to diverge the laser beam to a diameter of 8 mm on the surface. The height was relatively low to ensure sufficient light levels reached the camera. The speckles in the image are elongated in the x-direction due to motion blur as the stages were travelling in this direction at the time. This elongation is also apparent in the shape of the correlation peak. The blur itself doesn't introduce any error [29] into the measurement, however, the power in

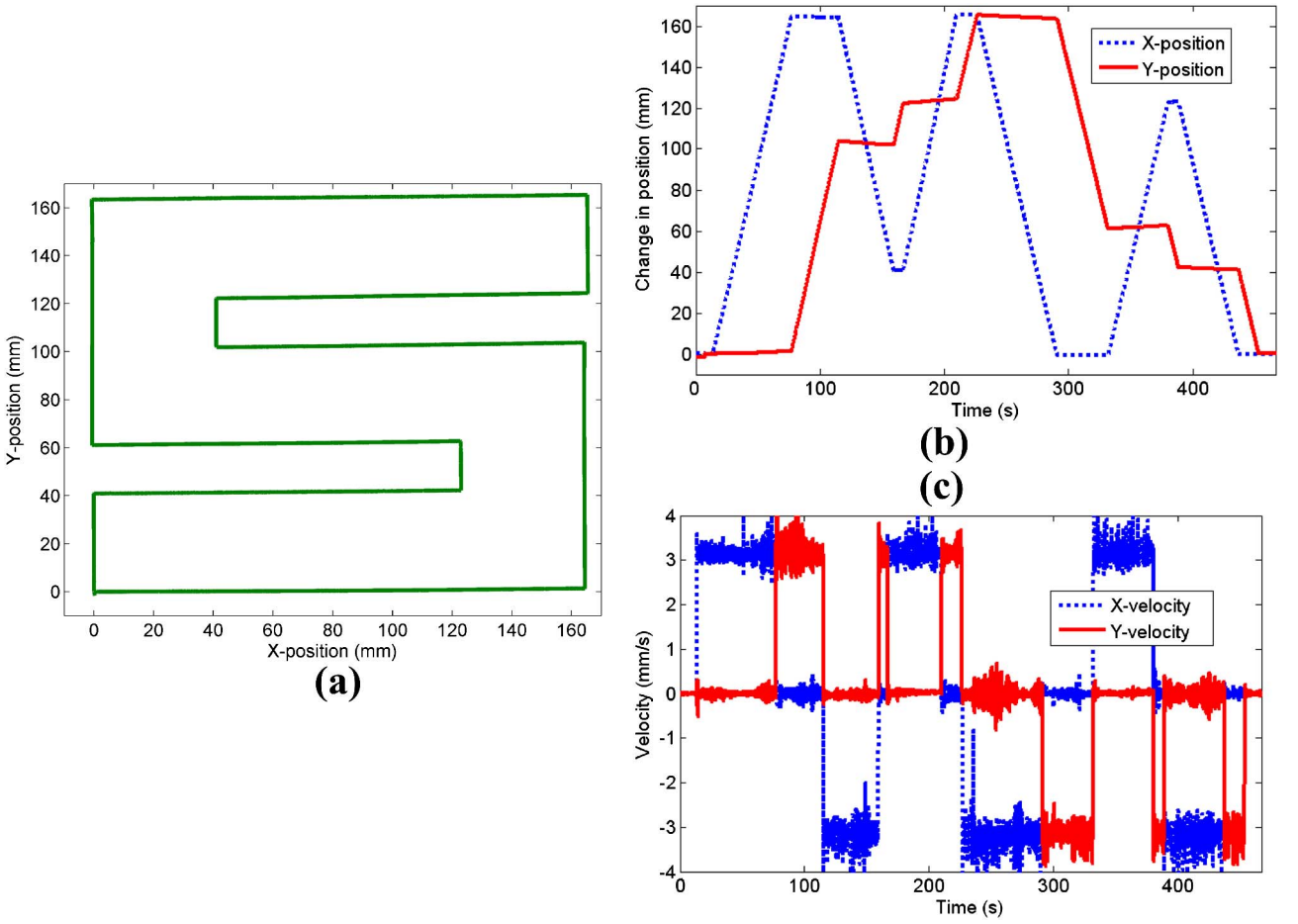

Fig. 11. (Color online) Path traversed (at 3 mm s^{-1}) calculated by integration of translation measurements from normalized crosscorrelation (a). The change in position (b) and velocity (c) of the x-axis stage (dashed-blue) and y axis stage (continuous-red).

the peak spreads over more pixels reducing the signal-to-noise ratio and increasing the likelihood of the correlation Q-factor falling below the threshold. The images were recorded at a frame rate of 1,000 FPS with an exposure time of 400 μs. The exposure time was chosen to provide a balance between limiting the motion blur enough that most correlation Q-values were above the threshold and providing enough signal to produce good contrast speckle patterns. The contrast here is not maximised though with about 140 out of 256 gray-levels used in the example shown. The Q-factor of the correlation peak shown is 16.03. The end position was measured to be (2.03, 3.32), a few millimeters out from the actual end point of (0,0), and corresponding a position error of 0.35% out of the total path of 1.12 m.

As a comparison, measurements were also made using subjective speckle. For this, the camera was fitted with a Sigma 28–70 mm zoom lens and a 0.6 mm aperture was used to provide an average speckle size approximately twice the pixel size. A 10× magnification microscope objective was used to diverge the laser beam to a diameter of 18 mm on the surface which overfilled the field of view and reduced the influence of the Gaussian beam profile. Figure 13(a) shows the path calculated from cross-correlation measurements of subjective speckle patterns when the stages are moving at a maximum velocity of 50 mm s^{-1}. It was difficult to get sufficient signal levels with the small aperture and widely divergent beam involved so a slower velocity was used here than in the previous example with objective speckle. The speckle patterns from a pair of successive frames in the movie file is shown in Fig. 13(b) and 13(c) and the normalized crosscorrelation between them is shown in Fig. 13(d). The field of view in each of the speckle patterns is 3.0 mm^2. The main qualitative difference between the subjective speckle patterns in Fig. 13 and the objective speckle patterns in Fig. 12 is that some of the surface features can be seen in the subjective speckle patterns due to it being imaged. The image of the surface features introduces some background energy into the correlation image resulting in noticeably lower typical correlation Q-values than observed with objective speckle. The example shown in Fig. 13(d) has a Q-value of 6.51. The Q-value threshold was therefore reduced to 2 for the subjective speckle measurements. Since the speckle pattern is imaged and the stages are moving slightly slower than in the objective example, a lower frame rate and longer exposure time were used. In this case the frame rate was 250 FPS and the exposure time was 1,400 μs. The final calculated

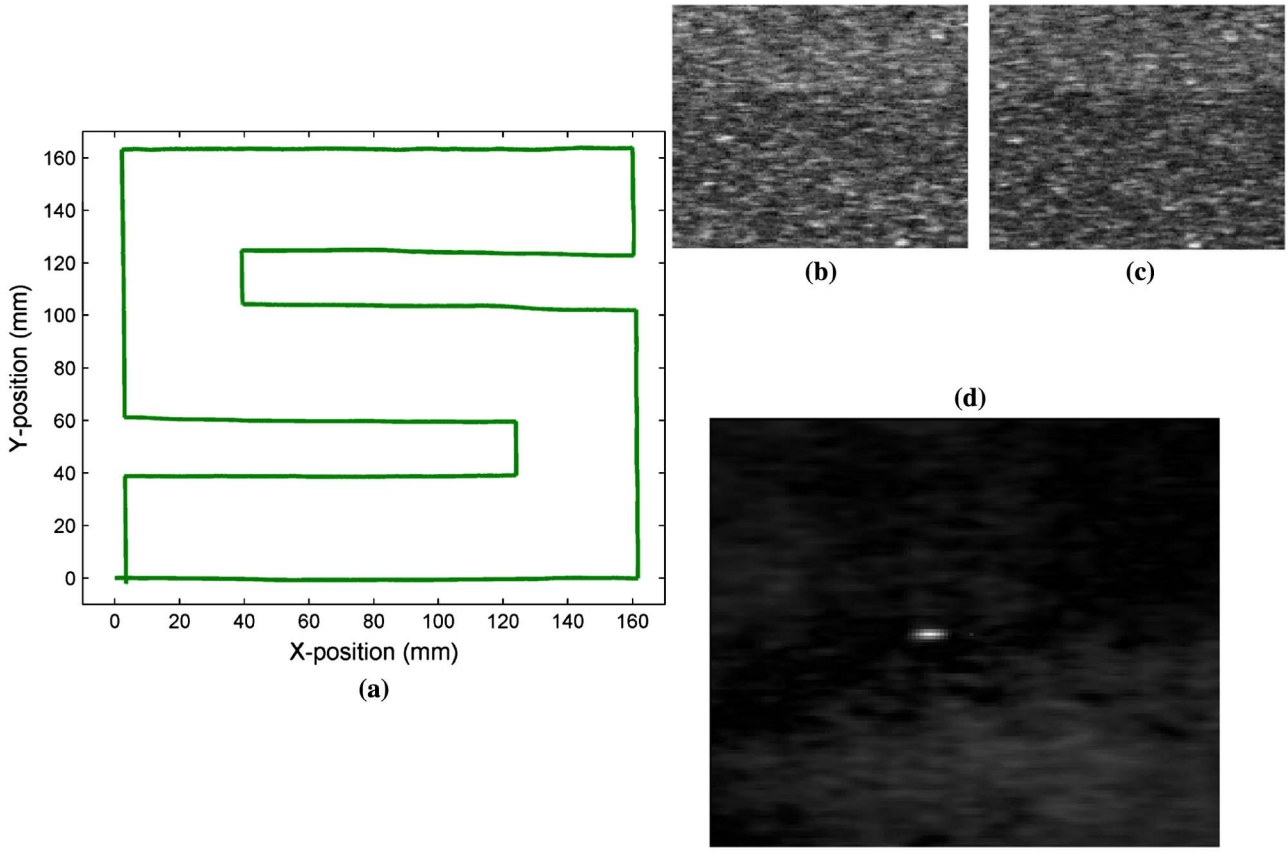

Fig. 12. (Color online) The path calculated by cross-correlation with the stages running at a maximum velocity of 80 mm s^{-1} (a). A pair of speckle patterns in successive frames at a point where the stages are moving at maximum velocity (b) and (c), and the normalized cross-correlation between them (d).

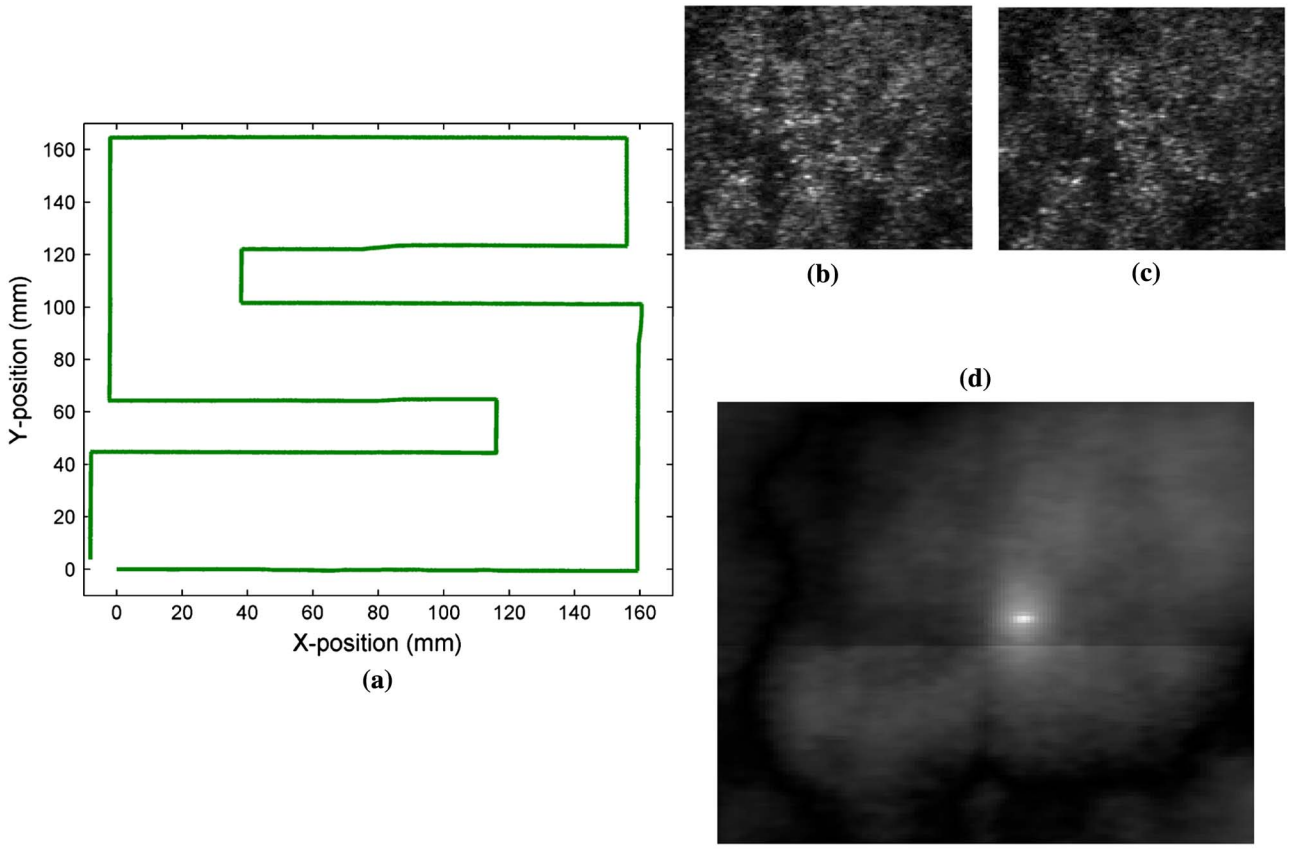

Fig. 13. (Color online) The path calculated by cross-correlation of subjective speckle patterns with the stages running at a maximum velocity of 50 mm s^{-1} (a). A pair of speckle patterns in successive frames at a point where the stages are moving at maximum velocity (b) and (c), and the normalized cross-correlation between them (d). The field of view in the speckle images is 3.0 mm^2.

Table 2. Summary of the Advantages and Disadvantages of Objective and Subjective Speckle

	Objective Speckle	Subjective Speckle
Advantages	Signal levels improve as camera moves closer to surface. Uniform background levels result in higher correlation Q-factors. Sensitivity can be adjusted by changing observation and viewing configuration.	Signal not dependent on camera surface separation, so could work better at long working distances, depending on optics. Scaling can be determined from field of view so no need to measure the observation and illumination positions.
Disadvantages	Scaling requires measurement of observation and illumination positions. Smaller beam diameter required to control speckle size results in better signal levels, but greater potential for blocking by objects.	Aperture to control speckle size obstructs a lot of available light. Non-uniform background due to Gaussian beam profile and imaged surface features result in reduced correlation Q-factors. Long telephoto imaging lens or beam shaping optics necessary to reduce effect of Gaussian beam profile.

position was (−8.15, 3.96) which corresponds to an error in position of 0.81%.

5. Discussion and Conclusion

In this paper, objective speckle velocimetry has been investigated for the purpose of determining odometry data on autonomous robotic vehicles. The influence of the geometry of the configuration on the speckle translation to vehicle translation scaling factor has been analysed using a computer model. As a result of this analysis, objective speckle velocimetry was found to be applicable by using measurements of the observation and illumination positions to determine the scaling factor. Objective speckle offers a number of advantages over subjective speckle for odometry, in particular, the reduction in the optical components required and the removal of the small aperture used to increase speckle size which reduces the available light in subjective speckle measurements. Also, the dependence of the scaling factor on the configuration also offers a simple way of adjusting the sensitivity of the instrument depending on

the application. Table 2 summarizes the advantages and disadvantages of the two techniques.

A test system was developed comprising a pair of linear translation stages and a sensor module consisting of a laser and a CMOS camera. The test system was used to verify the variation of scaling factor with object height observed during the modelling process. The process of verifying this variation revealed that minimizing the angle between the observation and illumination directions reduces the error in the scaling factor introduced by uncertainties in the measurements of the observation and illumination positions. Experimental measurements were presented at stage velocities much greater than we had previously been able to achieve [13], and are comparable to numerous autonomous vehicles to which the technique might be applicable. Tests were performed using both speckle types with an observed position accuracy of 0.35% for objective speckle and 0.81% for subjective speckle.

Further research is required to determine the influence of vehicle rotation on the correlation, but could be calculated using multiple sensors and the rotation coefficients present in Eq. (7). The effect of variation in surface height as the stages are moving and variation in the surface incidence angle are also the subject of future investigations. The normalized cross-correlation function could also be implemented using field programmable gate arrays (FPGA) which could be used in the development of more cost effective sensors. A correlation algorithm implemented on a FPGA has recently been reported [30] that is capable of 76 FPS for 512×512 images with a data rate of 20 MB s^{-1}, suggesting that over 1,000 FPS should be achievable for 128×128 images.

This study was funded by an Engineering and Physical Sciences Research Council (EPSRC) grant: Speckle velocimetry for high accuracy and multi-dimensional odometry (Grant No. EP/H019839).

References

1. J. Borenstein and L. Feng, "Measurement and correction of systematic odometry errors in mobile robots," IEEE T. Robotic. Autom. **12**, 869–880 (1996).
2. M. Maimone, P. C. Leger, and J. J. Biesiadecki, "Overview of the Mars Exploration Rovers' autonomous mobility and vision capabilities," Presented at the IEEE International Conference on Robotics and Automation (ICRA), Roma, Italy (14 April, 2007).
3. B. Gassmann, F. Zacharias, J. M. Zöllner, and R. Dillmann, "Localization of walking robots," in *IEEE International Conference on Robotics and Automation (ICRA)* (IEEE, 2005), 1471–1476.
4. S. Larionova, L. Marques, and A. T. de Almeida, "Detection of natural landmarks for mapping by a demining robot," *IEEE/RSJ International Conference on Intelligent Robots and Systems* (IEEE, 2006) 4959–4965.
5. P. G. de Santos, E. Garcia, J. Estremera, and M. A. Armada, "DYLEMA: using walking robots for landmine detection and location," Int. J. Syst. Sci. **36**, 545–558 (2005).
6. P. Hansen, H. Alismail, P. Rander, and B. Browning, "Monocular visual odometry for robot localization in LNG pipes," *2011 IEEE International Conference on Robotics and Automation (ICRA)* (IEEE, 2011), 3111–3116.
7. D. W. Seward and M. J. Bakari, "The use of robots and automation in nuclear decommissioning," in the 22nd International Symposium on Automation and Robotics in Construction (ISARC 2005) , Ferrara, Italy, 11–14 September, 2005.
8. D. Nistér, O. Naroditsky, and J. Bergen, "Visual odometry for ground vehicle applications," J. Field Robot. **23**, 3–20 (2006).
9. S. S. Beauchemin and J. L. Barron, "The computation of optical flow," ACM Comput. Surv. **27**, 433–467 (1995).
10. M. Maimone, Y. Cheng, and L. Matthies, "Two years of visual odometry on the Mars exploration rovers," J. Field Robot. **24**, 169–186 (2007).
11. H. Durrant-White, "Autonomous land vehicles," Proc. I. Mech. E. Part 1: J Systems Control Eng. **219**, 77–98 (2005).
12. A. Aliverdiev, M. Caponero, and C. Moriconi, "Some issues concerning the development of a speckle velocimeter," Tech. Phys+. **48**, 1460–1463 (2003).
13. T. O. H. Charrett, L. Waugh, and R. P. Tatam, "Speckle velocimetry for high accuracy odometry for a Mars exploration rover," Meas. Sci. Technol. **21**, 025301 (2010).
14. M. Sjödahl and L. R. Benckert, "Systematic and random errors in electronic speckle photography," Appl. Opt. **33**, 7461–7471 (1994).
15. J. C. Dainty, "The statistics of speckle patterns," *Progress Optics XIV*, E. Wolf, ed. (North Holland, 1976).
16. G. Cloud, "Optical methods in experimental mechanics, part 27: Speckle size estimates," Exp. Tech. **31**, 19–22 (2007).
17. J. P. Lewis, "Fast normalized cross-correlation," accessed 28/11/11, scribblethink.org/Work/nvisionInterface/nip.pdf.
18. H. Nobach and M. Honkanen, "Two-dimensional Gaussian regression for sub-pixel displacement estimation in particle image velocimetry or particle position estimation in particle tracking velocimetry," Exp. Fluids **38**, 511–515 (2005).
19. R. S. Sirohi, "Speckle interferometry," Contemp. Phys. **43** (3), 161–180 (2002).
20. M. Sjödahl, "Digital speckle photography," in *Digital Speckle Interferometry and Related Techniques*, P. Rastogi, ed. (Wiley, 2001).
21. P. Synnergren, "Measurement of three-dimensional displacement fields and shape using electronic speckle photography," Opt. Eng. **36**, 2302–2310 (1997).
22. I. Yamaguchi, "Speckle displacement and decorrelation in the diffraction and image fields for small object deformation," Opt. Acta **28**, 1359–1376 (1981).
23. M. Hrabovský, Z. Bača, and P. Horváth, "Theory of speckle displacement and decorrelation and its application in mechanics," Opt. Laser Eng. **32**, 395–403 (2000).
24. P. Horváth, M. Hrabovský, and P. Šmíd, "Full theory of speckle displacement and decorrelation in the image field by wave and geometrical descriptions and its application in mechanics," J Mod. Opt. **51**, 725–742 (2004).
25. P. Horváth, M. Hrabovský, and P. Šmíd, "Application of speckle decorrelation method for small translation measurements," Opt. Appl. **34**, 203–218 (2004).
26. P. Šmíd, P. Horváth, and M. Hrabovský, "Speckle correlation method used to measure object's in-plane velocity," Appl. Opt. **46**, 3709–3715 (2007).
27. "Red sand texture," accessed 28/11/11, http://killcaiti-stock.deviantart.com/art/Red-Sand-Texture-87316332.
28. "Fastest Fourier transform in the west," accessed 28/11/11, http://www.fftw.org/download.html.
29. G. E. Elsinga, B. W. van Oudheusden, and F. Scarano, "The effect of particle image blur on the correlation map and velocity measurement in PIV," Proc. SPIE **5880**, 588010 (2005).
30. J. Ding, X. Du, X. Wang, and J. Liu, "Improved real-time correlation-based FPGA stereo vision system," in the *2010 IEEE International Conference on Mechatronics and Automomation (ICMA)* (IEEE, 2010), 104–108.